

Supporting Information for

Two-Dimensional Porous Electrode Model for Capacitive Deionization

Ali Hemmatifar,¹ Michael Stadermann,² and Juan G. Santiago*¹

¹ Department of Mechanical Engineering, Stanford University, CA 94305, USA

² Lawrence Livermore National Laboratory, 7000 East Avenue, Livermore, CA, USA

* To whom correspondence should be addressed. Tel. 650-736-1283, Fax 650-723-7657, E-mail:
juan.santiago@stanford.edu

This document contains Supplementary Information and figures describing design aspect of our desalination cell and further discussion on CDI system dynamics.

Contents

S1. Effect of electrode compression on contact resistance.....	2
S2. Macropore concentration plots for low and high inlet concentration	3
S3. Micropore concentration plots and evidence of shockwave.....	5
S4. Diffusion flux and salt adsorption rate	6
S5. Macropore potential and micropore charge state	6
S6. Note on potential boundary condition	7
S7. Movies of macro- and micropore salt concentration.....	9
References.....	9

S1. Effect of electrode compression on contact resistance

As we mentioned in the main text, in addition to the effect of conductive epoxy on the system resistance, we observed that electrode compression can significantly improve the electrode-to-current-collector contact. We quantified the effect of compression force on this contact resistance using *ex situ* voltage-current readings and comparison of these to pressure force exerted on the stack of electrode-current collector by fasteners. We found 3 to 4 times reduction in contact resistance at ~ 100 kPa pressure. A recent study¹ suggests that this is because compression increases the number and quality of microscopic point contacts.

We show three-dimensional isometric drawings of the two major components of our desalination cell flow structure in Figure S1. Our design included four compression slot features (see Figure S1a) which we use to improve the contact between the electrodes and current collectors. As shown in the figure, these slot features are implemented together with a set of plastic shim features (labeled “plastic pieces” in Figure S1b). Upon sealing of the two major halves of the cell, these shims create four regions of high compression (they “pinch” the “wings” of the electrodes within the slot features). We found that, upon assembly, these four pinched regions decrease the contact resistance by a factor of 3 to 4. We hypothesize that these four peripheral compression regions leave the large majority of the central electrode regions unchanged.

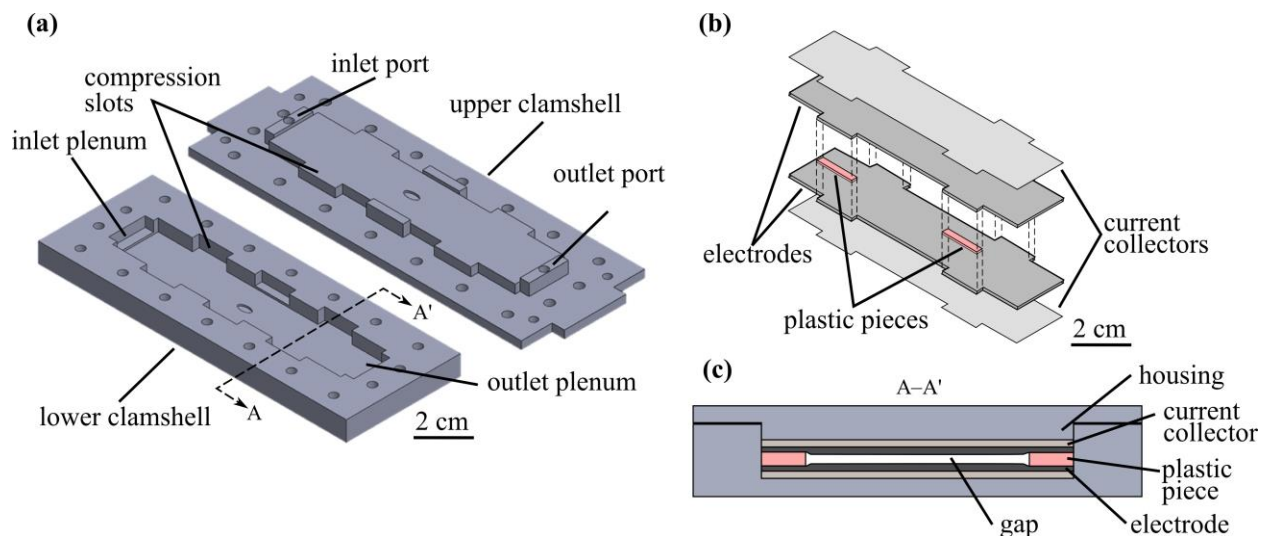


Figure S1 (a) Three-dimensional drawing of CDI cell clamshell structure. We sandwiched a pair of activated carbon electrodes inside the upper and lower clamshells and sealed the desalination cell using gasket and fasteners. Electrodes have dimension of 100×20 mm with 0.68 mm thickness. Our design had compression slots we used to compress outer regions of the electrode upon assembly. This technique led to 3- to 4-fold decrease in contact resistance. (b) Cross-section schematic of stack of activated carbon electrodes between stainless steel current collectors. Current collectors were bonded to backside of the electrodes by silver epoxy. We placed thin frames of plastic between the electrodes to avoid the electrodes touching each other. (c) Cross sectional view of the assembled cell.

S2. Macropore concentration plots for low and high inlet concentration

Figures S2 and S3 show line plots of macropore concentration for 20 and 200 mM inlet concentration cases. Figures S2a/S3a and S2b/S3b respectively present ion concentrations in macropores along the line $\bar{x} = 1/2$ during charging and discharging processes. In Figure S2, as charging progresses, counterions are adsorbed to micropores while co-ions are expelled. In the early phase of charging (gray contours), counterions are transported within the electrode *via* both electromigration and diffusion. In this phase, nonlinear coupling of ion adsorption, diffusive transport, and electromigration mechanisms create a local concentration minimum near the interface. This local minimum propagates through the electrode until ions in the macropore are largely depleted by circa $\bar{t} = 1$ (electrode starvation). Charging continues subsequent to $\bar{t} = 1$ but at a rate which is progressively more limited by diffusion. This results in linear profiles near the $\bar{y} = L_s/2L_e$ boundary of the electrode as primarily diffusive transport supplies new ions to the electrode volume.

The initial rapid ($\bar{t} = 14$ to 15) and subsequent diffusion-limited transport phases of discharge are shown in the gray and black contours of Figure S2b, respectively. The combined electromigration-diffusion-accumulation dynamics here result in a local concentration maximum near the gap which propagates into the electrode. This is followed by a long-duration, diffusive transport of ions out of the electrode.

On the other hand, electrode starvation is not observed for the high concentration case (see Figure S3). However, time scales associated with the early charging as well as discharging phase are similar to low concentration case. Additionally, the concentration profiles in discharging process are quite similar to 20 mM case.

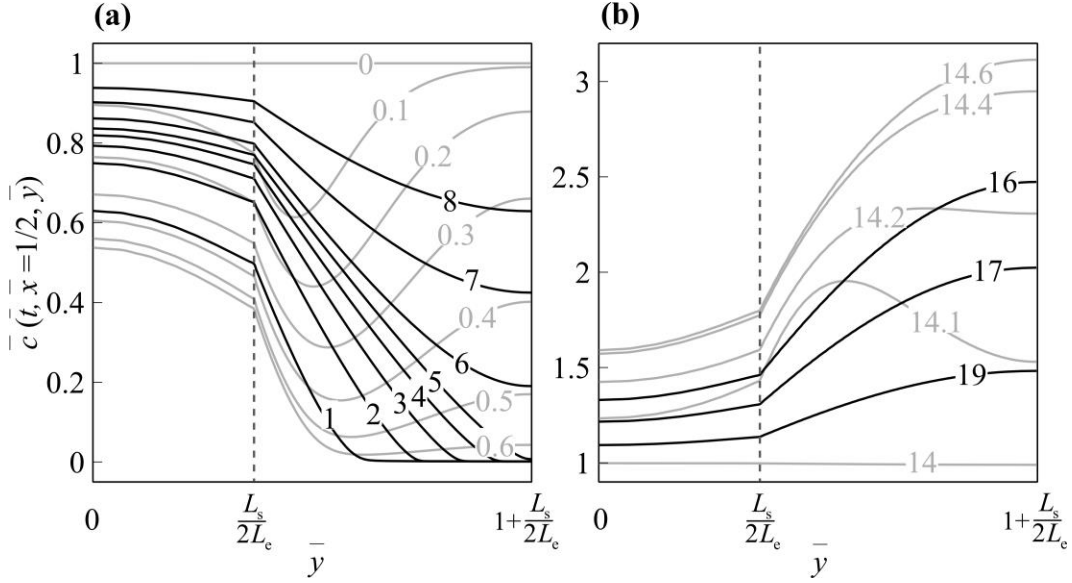


Figure S2 Ion concentration in gap and macropores normalized by 20 mM inlet concentration along the line $\bar{x} = 1/2$ in constant voltage (a) charging and (b) discharging under conditions similar to those of Figure 6 of the main text. Vertical dashed line denotes the electrode interface and results are shown for upper-half of the system. Gray lines represent concentration profiles shortly after starting charging or discharging, and black lines show concentration evolution at longer times. Each line is labelled with corresponding non-dimensional time (scaled by L_e^2/D_e).

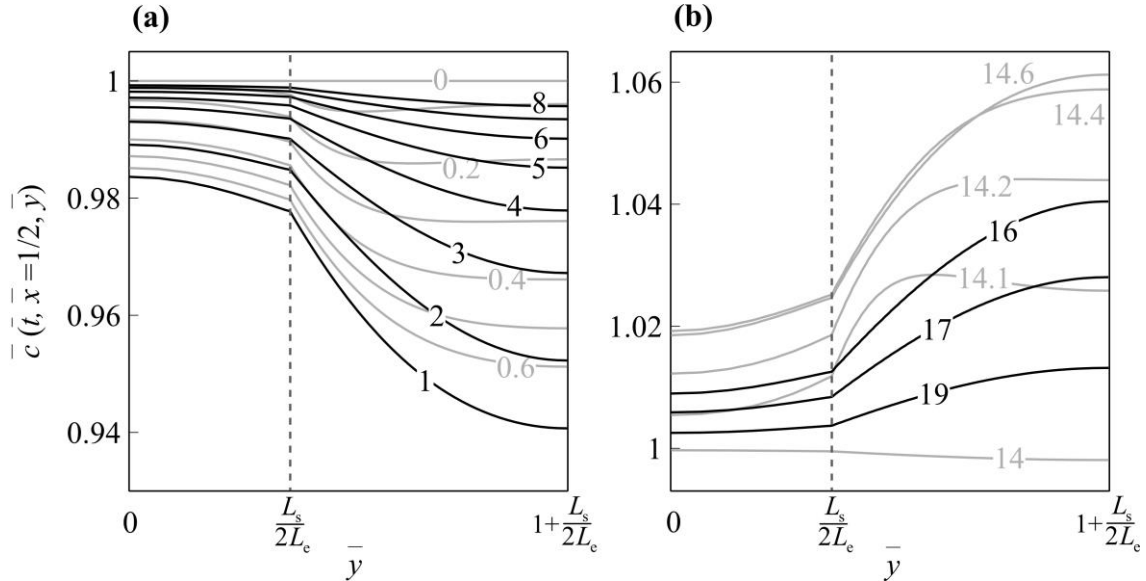


Figure S3 Ion concentration in gap and macropores normalized by 200 mM inlet concentration along $\bar{x} = 1/2$ for constant voltage (a) charging and (b) discharging under conditions similar to those of Figure 7 of the main text. The label for each curve corresponds to time nondimensionalized by L_e^2/D_e . In contrast to Figure S2a, electrode starvation is not observed. However, early charging as well as discharging have time scales analogous to 20 mM case. Moreover, concentration lines for the discharge process are qualitatively similar to 20 mM case.

S3. Micropore concentration plots and evidence of shockwave

Normalized micropore counterion concentration throughout the upper-electrode in charging process for 20 mM inlet salt concentration is presented in Figure S4. Figure S4a shows that the counterion concentration within near-interface micropores increases to $\bar{c}_m^+ \approx 30$ within about $\bar{t} = 1$ (compare to the fully charged state of $\bar{c}_{m,\max}^+ \approx 35$). During this time, the counterion concentration at the collector boundary ($\bar{y} = 1 + L_s/2L_e$) increases to $\bar{c}_m^+ \approx 10$ but then remains approximately “pinned” near this value from about $\bar{t} = 10$ to 4, indicating only partially charged micropores throughout much of the near-collector region of the electrode. The location of the steep-gradient between this near-interface value of $\bar{c}_m^+ \approx 30$ and the near-collector value of $\bar{c}_{m,\max}^+ \approx 10$ then propagates toward the collector as ions diffuse into this region and adsorb. The interplay between diffusion and concentration-dependent adsorption rate results in a sharpening of the concentration interface. We later discuss this phenomenon in more detail (c.f. Figure S5 for a plot of diffusive transport vs. adsorption rate). This sharpening results in what appears to be a propagating micropore ion concentration shock wave which propagates through the electrode at these conditions.

The micropore counterion concentration of the discharge process is shown in Figure S4b. As described above, diffusion and electromigration mechanisms result in an initially rapid depletion of counterion concentration. This is then followed by a slow diffusion-limited expulsion of ions.

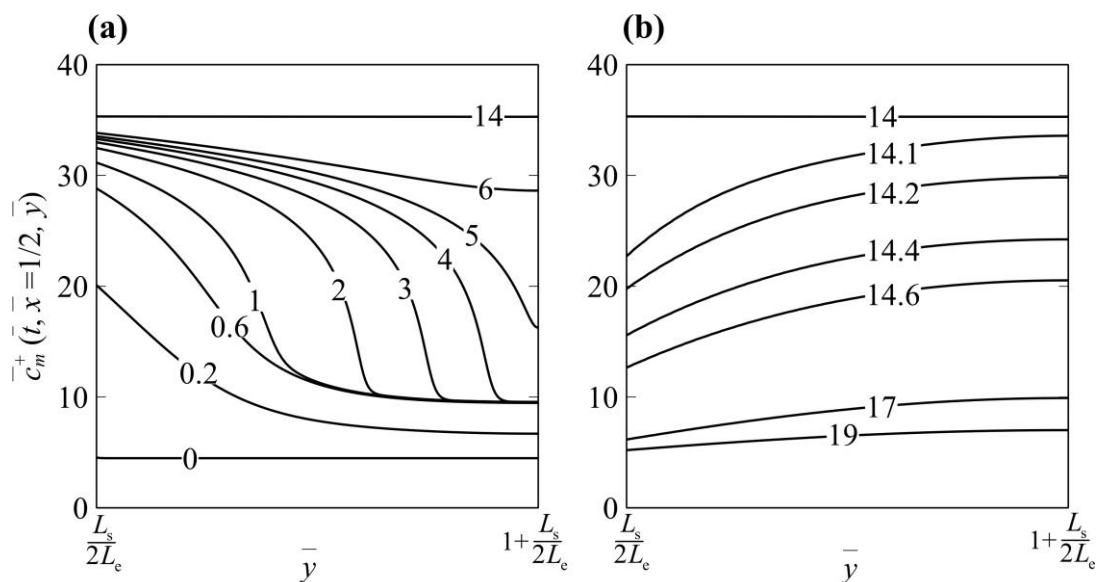


Figure S4 Normalized micropore counterion concentration along $\bar{x} = 1/2$ for constant voltage (a) charging and (b) discharging (under the charging conditions of Figure 2). The degree of charge of micropores near the interface quickly increases to 85% (corresponding to $\bar{c}_m^+ \approx 30$). Counterion diffusion (from bulk) and adsorption to partially-charged micropores sharpens gradient between the low- and high-charge state zones, and apparently forming a moving shock which slowly propagates toward the collector. The process continues until micropores are filled. Discharging shows an initially rapid expulsion of ions, followed by a slow, diffusive expulsion.

S4. Diffusion flux and salt adsorption rate

We here further discuss diffusion limitations of charge transport. Figures S5a and S5b respectively show normalized directional diffusion flux $-\partial\bar{c}/\partial\bar{y}$ and local (instantaneous) salt adsorption rate $\partial\bar{w}_m/\partial\bar{t}$ along $\bar{x}=1/2$ within the electrode at selected times during charging. Figure S5a shows how the diffusive flux distribution quickly (within about \bar{t} of unity) forms a step-like function, with a rapid drop in flux within the electrode. This high gradient flux feature then propagates toward the current collector. Comparison of Figures S5a and S5b show that this step function in flux coincides with a spatial peak in adsorption rate. This is expected as the “sink function” of adsorption results in a rapid change in flux. To the left of this adsorption peak, the micropores approach saturation. To the right, micropores are starved and are forced to “wait” for the propagating front. Interestingly, the diffusion and adsorption dynamics couple to create what is apparently an ion concentration shockwave (see section 5.3 of main text).

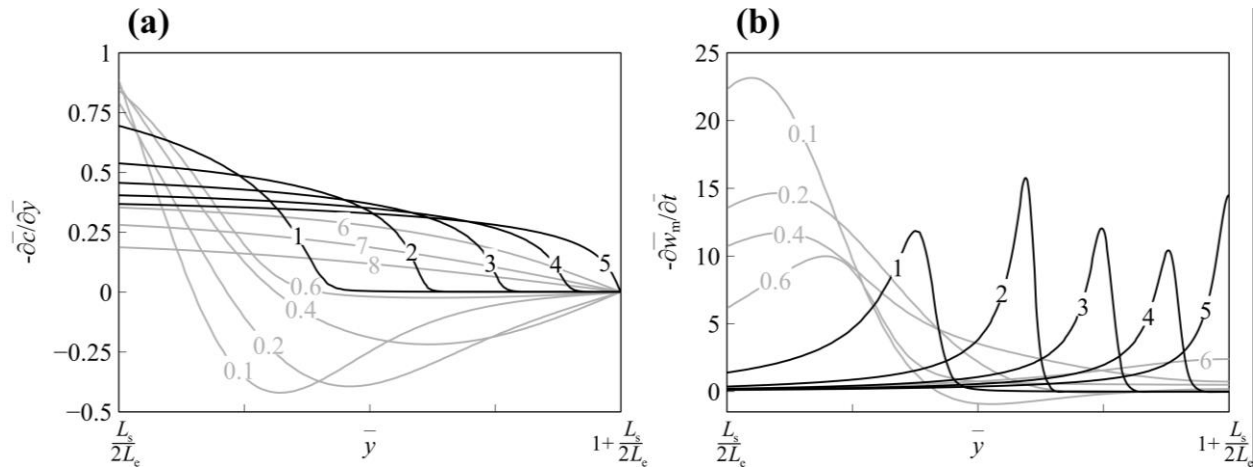


Figure S5 Normalized (a) diffusion flux in y-direction and (b) local salt adsorption rate along the line $x=1/2$ during charging process. (a) Shows the formation of a step-like distribution of diffusion flux (after time $\bar{t}=1$), and this feature propagates to the right. Coincident with this step feature is a corresponding local peak in adsorption rate. This peak in adsorption rate occurs at the left boundary of the shrinking starvation region.

S5. Macropore potential and micropore charge state

As follows from discussion in the main text, the local macropores potential can be indicator of micropores charge state. This is because a higher potential drop from electrode surface to macropores implies greater the stored charge in micropores (c.f. eq 13 of the main text). In Figures S6a and S6b, we present the gap and macropore potential along $\bar{x}=1/2$ in charging and discharging processes, respectively (reference potential located at $y=0$). Figure S6a shows that upon application of 1 V to the system (0.5 V and -0.5 V potentials at the two electrodes), potential of near-collector macropores quickly drops to $\sim 7V_T$ and remains approximately pinned at this

value from $\bar{t} \approx 1$ to 4. So, from a total potential of $\sim 20V_T$ dropped from each electrode to centerline (the 0.5 V value) about 65% is taken by combination of Donnan and micropore potential drops, $\Delta\phi_D + \Delta\phi_m$ (c.f. section 2.1 of the main text for more information). This means that the micropores are capable of adsorbing additional ions, but the near-collector regions of electrode are starved during this time (see Figure S4a). As micropores are being slowly charged, the macropore potential approaches zero and hence $\Delta\phi_D + \Delta\phi_m$ approaches $20V_T$. Note, in the absence of Faradaic reactions (as Figures S6a and S6b show) the equilibrium condition for either charging or discharging is uniformly zero macropores potential.

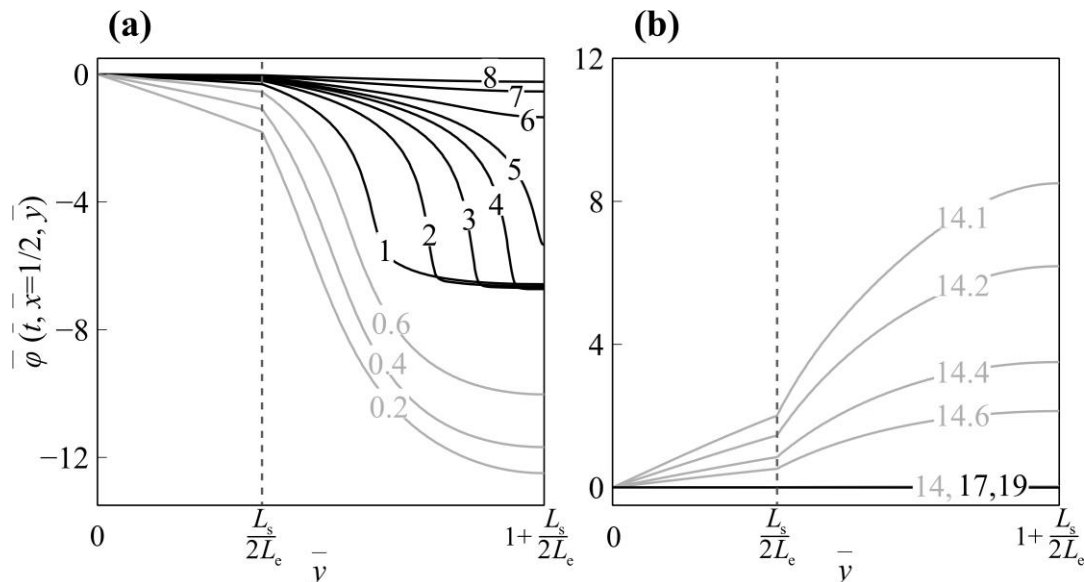


Figure S6 Gap and Macropore potential (normalized by thermal voltage) along $\bar{x} = 1/2$ during (a) charging and (b) discharging processes (under the charging conditions of Figure S2). In charging, initial macropore potential at the near-collector region quickly drops to $\sim 7V_T$ and remains approximately pinned near this value from $\bar{t} = 1$ to 4 (consistent with partially charged micropores). Potential drops to zero throughout the electrode as micropores fully charge (at about $\bar{t} = 8$). During discharge, macropore potential quickly increases and is positive as net charge is released. Macropore then relaxes back to zero as the electrode is discharged.

S6. Note on potential boundary condition

We here discuss our choice of boundary conditions (BCs) for electric potential. We show our model is insensitive to the choice of BC at the inlet and outlet regions. This is an intended and direct result of our use and implementation of extended inlet and outlet flow regions of the domain. In most experimental CDI cells, there are standoff regions in the form of inlet and outlet tubing upstream and downstream of the cell. The distance between external ground nodes (*e.g.*, metal connection touching electrical ground) are typically made sufficiently far from the cell so as to not

interfere with the cell's operation. We capture this characteristic in our model by adding extended inlet and outlet flow regions to our solution domain (see Figure 1b of the main text).

The potential in the inlet, outlet, and spacer regions of our cell is governed by a nonlinear Laplace equation of the form $\nabla \cdot (c \nabla \phi) = 0$ (since conductivity is not uniform), as discussed in section 2.2 of the main text. Unique solutions to this require at least one Dirichlet boundary condition (BC). One Dirichlet BC for potential in our model is the symmetry line (which is extended along the lower edge of computational domain). This Dirichlet BC is sufficient to specify the unique solution of the potential. By using extended inlet/outlet sections, we make our model insensitive to the specific choice (or values) of BCs at the inlet ($x = -L/8$) and outlet ($x = L + L/8$). Hence, our BC at inlet/outlet can be either $\phi = 0$ or $\partial\phi/\partial x = 0$. We chose $\phi = 0$ at these boundaries as a simple, convenient choice.

To validate our choice, we solved our model for all four possible cases ($\phi = 0$ or $\partial\phi/\partial x = 0$ at either/both inlet or outlet) and confirmed that our solutions are insensitive to this. We further validated this idea by evaluating various lengths of inlet and outlet domains. The latter work showed negligible change in the solution for increases of inlet and outlet domain lengths beyond our chosen values.

We illustrate this point using the Figure S7 below. Here we show the potential along $y = L_s/4$ evaluated at time $t = 20$ s. Parameter settings are similar to those in Figure 6 of the main text. Figure S7 shows overlap of all solutions for the four choices of boundary conditions at the extreme boundaries of our inlet and outlet conditions.

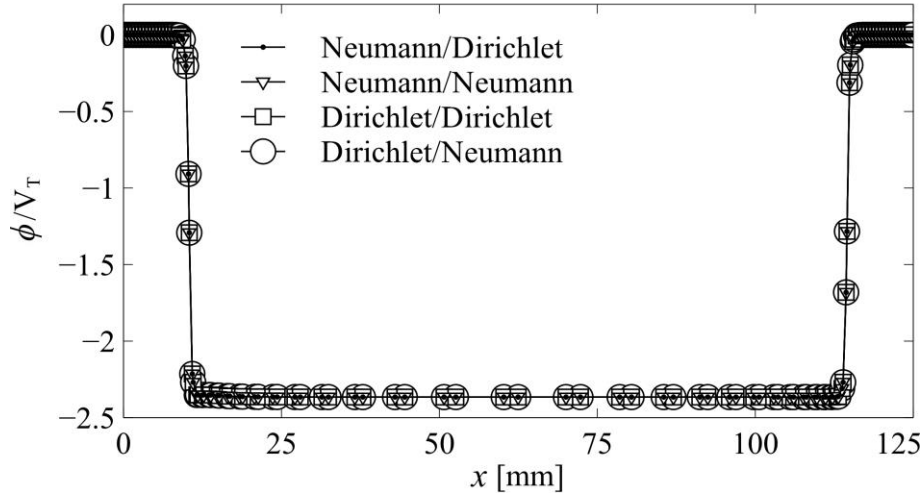


Figure S7 Normalized potential in the inlet, outlet, and spacer regions along $y = L_s/4$ at time $t = 20$ s for four possible choice of BCs at inlet and outlet. Results show overlap of all solutions. Parameter settings are similar to those in Figure 6 of the main text.

S7. Movies of macro- and micropore salt concentration

This Supplementary Information includes two movies showing spatiotemporal field data for concentration in the macro- and micropores. Specifically, the movie titled “macropore concentration” shows normalized concentration field in macropores, spacer, and inlet and outlet sections ($\bar{c}(x, y, t)$) during charging and discharging processes. Similarly, the movie titled “counterion micropore concentration” shows normalized counterion concentration field in the electrode micropores ($\bar{c}_m^+(x, y, t)$). Parameter settings used are to the same as those of Figure 6 of the main text. Inlet concentration in each movie is normalized by inlet concentration (20 mM).

References

- (1) Qu, Y.; Baumann, T. F.; Santiago, J. G.; Stadermann, M. Characterization of Resistances of a Capacitive Deionization System. *Environ. Sci. Tech.* **2015**, *49* (16), 9699–9706.